Mutations Decouple Proton Transfer from Phosphate Cleavage in the dUTPase Catalytic Reaction

Anna Lopata,[†,¶] Pablo G. Jambrina,[‡] Pankaz K. Sharma,[§,#] Bernard R. Brooks,[∥] Judit Toth,[*,†] Beata G. Vertessy,[*,†,⊥] and Edina Rosta[*,‡]

[†]Institute of Enzymology, Research Centre for Natural Sciences, Hungarian Academy of Sciences, Budapest H1113, Hungary

[‡]Department of Chemistry, King's College London, London SE1 1DB, United Kingdom

[§]College of Pharmacy, Graduate School of Pharmaceutical Sciences, Ewha Womans University, Seoul 120-750, Korea
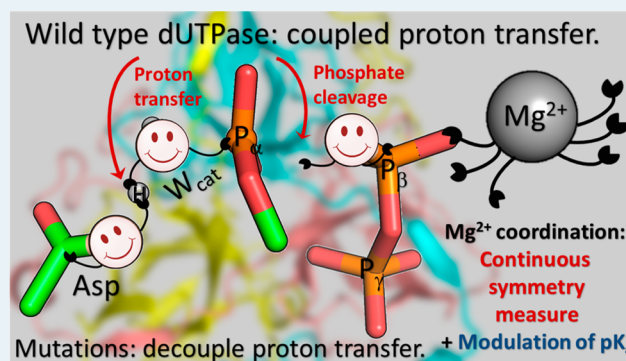
[∥]Laboratory of Computational Biology, National Heart, Lung, and Blood Institute, National Institutes of Health, Rockville, Maryland 20892-9314, United States

[⊥]Department of Applied Biotechnology and Food Science, Budapest University of Technology and Economics, Budapest H1111, Hungary

Ⓢ *Supporting Information*

ABSTRACT: Most enzymes present a catalytic mechanism where one or more proton transfer events occur coupled tightly together with the enzymatic chemical reaction. We show here that inactivating mutations decouple this proton transfer step from the phosphate cleavage reaction in dUTPase. Homotrimeric dUTPase enzymes catalyze the hydrolysis of dUTP to dUMP and pyrophosphate, using largely similar structural and functional groups as most AAA+ enzymes. dUTPases typically use a single Mg^{2+} ion as a cofactor in the active site that is formed by direct protein–protein contacts including all three protomers. Here we focus on the C-terminal arm structural motif, which has sequence and functional similarities to P-loop motifs and is required for catalysis. In this work, we have studied the functional roles of the C-terminal arm in ligand binding and catalysis by using QM/MM (quantum mechanics/molecular mechanics) calculations in conjunction with site-directed mutagenesis experiments. We also present a new method to assess the metal ion coordination symmetry during the catalytic reaction. Using this new implementation, we identified that the coordination symmetry follows a consistent pattern in the three systems studied, reaching the most symmetrical state near the transition states. We found that the phosphate cleavage proceeds with a concerted bimolecular (A_ND_N) mechanism with a loose dissociative transition state and that it is coupled with a proton transfer step involving a unanimously conserved Asp residue. We show that the main mechanistic effect of the lack of the C-terminal arm is to decouple the phosphate cleavage from the subsequent proton transfer step, resulting in a high-barrier altered reaction pathway.

Wild type dUTPase: coupled proton transfer.
Proton transfer — Phosphate cleavage
Mg^{2+}
Mg^{2+} coordination: Continuous symmetry measure + Modulation of pK_a
Mutations: decouple proton transfer.

KEYWORDS: QM/MM (quantum mechanics/molecular mechanics), dUTPase, continuous symmetry measure, one-metal ion catalytic mechanism, ab initio, DFT (density functional theory), coupled proton transfer

INTRODUCTION

The dUTPase (deoxyuridine triphosphate nucleotidohydrolase) enzymes catalyze the hydrolysis of dUTP (deoxyuridine triphosphate) to dUMP (deoxyuridine monophosphate) and pyrophosphate to avoid incorporation of uracil into the DNA instead of thymine and to provide the dUMP precursor for *de novo* dTTP (deoxythymidine triphosphate) biosynthesis.[1] An additional enzymatic activity, deamination of dCTP (deoxy-cytidine triphosphate) to dUTP, may also be carried out by bifunctional dUTPases in *Archaea*[2−5] and also in *Mycobacterium tuberculosis* (*M. tuberculosis*), which also has a monofunctional dUTPase.[6] The dUTPases comprise two structurally different classes:[7] first, the β sheet-type dUTPases, possessed by most organisms, employ a one-metal ion catalytic mechanism,[8,9] and

usually form a homotrimer[10] or a monomer,[11] while the second class, the α helical-type dUTPases, possessed by kinetoplas-tids,[12] form dimers and employ a two-metal ion catalytic mechanism.[13,14]

In β sheet-type trimeric dUTPases, each active site is constituted from motifs of all three protomers, which are all required to interact for achieving proper enzymatic activity.[15,16] These dUTPases have a C-terminal arm structural motif that has sequence similarity to P-loop motifs[17] also present in triphosphate hydrolysis catalyzing enzymes including kinases,
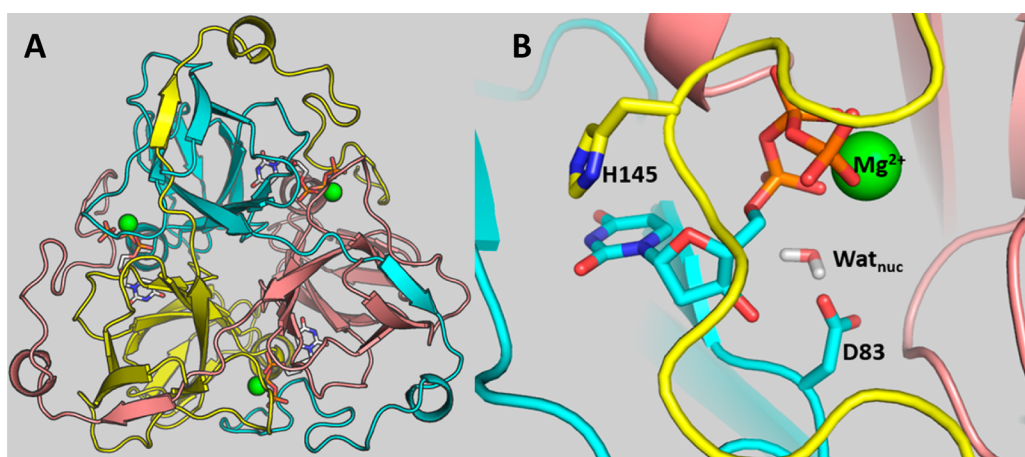
Figure 1. (A) Homotrimeric structure of the biological *M. tuberculosis* dUTPase assembly. Each active site consists of all the three protomers (yellow, cyan, and salmon cartoon), a dUTP molecule (sticks with atomic coloring), and a single Mg^{2+} ion cofactor (green sphere). (B) Active site of *M. tuberculosis* dUTPase from the WT simulation system. H145 (sticks) forms $\pi-\pi$ interactions with the uracil base of the substrate dUTP (sticks) at the interface of the three protomers, interacting with all the three chains (yellow, cyan, and salmon cartoon).

motor proteins, and membrane pumps.[18−20] In addition to the key C-terminal arm, the requirement of divalent metal ion cofactors for efficient catalysis is also shared by AAA+ (ATPases associated with diverse cellular activities) enzymes in general, commonly a single Mg^{2+} coordinating the phosphate groups of the substrate. Substitution of this Mg^{2+} with Ca^{2+} generally results in substantial loss of activity,[21,22] with only a few exceptions reported (e.g., for human endogenous retrovirus (HERV-K) dUTPases).[23] The P-loop-like C-terminal arms, the Mg^{2+} ion bound triphosphate nucleotides, and the binding interface of the remaining two protomers all contribute to the resulting three active sites of the native dUTPase complex.

   Here, we focus on the role of the C-terminal arm of *M. tuberculosis* dUTPase (Figure 1A) in the catalytic activity and in ligand-binding properties. We use both computationally intensive, accurate mixed quantum mechanics/molecular mechanics (QM/MM) calculations[24] and site-directed muta-genesis experiments. We study the wild-type (WT) dUTPase, a mutant lacking the entire C-terminal arm (denoted by T138Stop), and a second mutant including only a H145A mutation. The C-terminal arm structural motif has several conserved residues (Figure 2), one of which, His145, has well-conserved aromatic $\pi-\pi$ interactions with the nucleobase of the substrate.[17,25,26] His145 has a prominent location in the dUTPase active site: it interacts simultaneously with both the other two protomers and the substrate (Figure 1B). Deletion of the full C-terminal arm results in major activity loss for the T138Stop enzyme. The His to Ala mutation H145A preserves substrate binding; however, the catalytic rate decreases by a factor of 10. The measured binding affinities and catalytic rates of the T138Stop and H145A enzymes are consistent with the essential role of the C-terminal arm in other dUTPase proteins investigated.[17,25,27−32]

   To better understand the underlying energetic and structural causes determining the catalytic activity, we carried out QM/MM calculations of the reaction mechanism for proton transfer and phosphate cleavage in the WT and the two mutant (H145A and T138Stop) enzyme complexes. We recently identified a one-step associative A$_N$D$_N$ catalytic mechanism for the hydrolysis at the α-phosphate, involving also a coupled proton transfer step from the nucleophilic water to the catalytic Asp83 residue.[33] Here we show that essentially the same
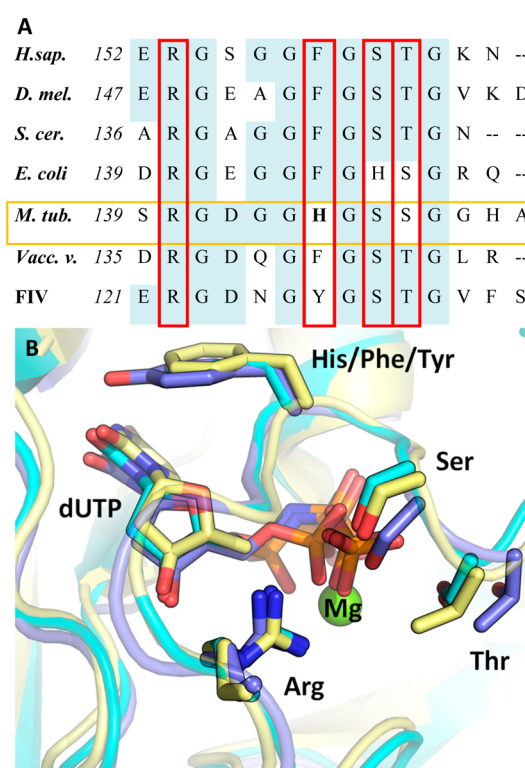

Figure 2. (A) Clustal W alignment of the C-termini of dUTPases from widely different species: human (*Homo sapiens, H. sap.*), *Drosophila melanogaster* (*D. mel.*), *Saccharomyces cerevisiae* (*S. cer.*), *E. coli, M. tuberculosis, Vaccinia virus* (*Vacc. v.*), and feline immunodeficiency virus (FIV). The conserved residues coordinating the dUTP are shown within a red frame. (B) Superimposed structures of the active sites of human, mycobacterial and FIV dUTPases (PDB IDs: 3EHW (unpublished), 2PY4,[26] and 1F7R,[36] respectively). The conserved residues coordinating the dUPNPP molecule, which is a slowly hydrolyzable dUTP analogue, are shown as sticks, protein shown as cartoon (yellow, cyan, and dark blue, respectively). Note that the presented FIV dUTPase structure contains dUDP with trans conformation instead of dUPNPP, and there is no Mg^{2+} ion coordinated to the phosphate chain of the substrate analogue.

mechanism takes place in all three dUTPase systems investigated. The coupled proton transfer and the phosphate
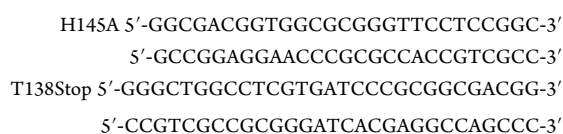
cleavage occur in a single step that has a loose dissociative transition state (TS) structure. The proton transfer directly follows the phosphate bond breaking, and it is coupled together with the new phosphorus—oxygen bond formation at the TS for the WT. For the H145A and T138Stop enzymes, the proton transfer is decoupled from the phosphorus—oxygen bond formation at the TS, in particular for the nearly inactive T138Stop dUTPase. In addition, we also found evidence that the specific metal ion coordination mode may play a prominent role. We analyzed the metal ion coordination during the reaction by calculating a continuous symmetry measure for the Mg^{2+}-ion coordination.[34] Changes in charge distributions of the three systems for the TS structures also reveal relevant differences in the partial charge transfer from the protein to the substrate due to the missing native protein—protein and protein—substrate interactions.

Our QM/MM calculations offer unique insights into the structural and electronic changes taking place along the catalytic reaction and, in conjunction with the experimental data, provide evidence on the crucial role of the dUTPase C-terminal arm in modulating ligand binding geometry and catalytic activity.[35]

■ MATERIALS AND METHODS

Experimental Methods. *Reagents.* Molecular biology products were obtained from New England Biolabs (U.S.A.) and Fermentas (Canada), electrophoresis and chromatography reagents were from Bio-Rad (U.S.A.) and Qiagen (Netherland). Phenol red was from Merck (Germany), dUDP and dUPNPP (α,β-imido-dUTP) was from Jena Bioscience (Germany); dUTP and other chemicals were from Sigma-Aldrich (U.S.A.).

Mutations on the C-Terminal Arm. C-terminal arm mutants have been generated to elucidate the roles of protein—protein and protein—substrate interactions of this conserved arm motif on dUTPase function. Two mutants were generated (H145A and T138Stop) focusing on the conserved residue of His145 (Figures 1 and 2) and a mutant lacking the last 17 residues of the C-terminal arm. Site-directed mutagenesis was performed by Stratagene's QuikChange method and was verified by sequencing. Mutagen forward and reverse primers were the following:

H145A 5′-GGCGACGGTGGCGCGGGTTCCTCCGGC-3′

5′-GCCGGAGGAACCCGCGCCACCGTCGCC-3′

T138Stop 5′-GGGCTGGCCTCGTGATCCCGCGGCGACGG-3′

5′-CCGTCGCCGCGGGATCACGAGGCCAGCCC-3′

Cloning, Protein Expression, and Purification. Cloning, protein expression, and purification were performed as described previously in Varga et al.[26] and as follows. Recombinant dUTPase with an N-terminal 6xHis-tag was expressed in *E. coli* strain BL21(DE3)pLysS. The final supernatant after cell extraction was loaded on a Ni-NTA column (Novagen) and purified according to the Novagen protocol. His-tag purification allows for specific purification of the recombinant proteins from the endogenous one. Protein concentration was measured using the Bradford method (Bio-Rad Protein Assay) and is given in monomers. Proteins were dialyzed against a buffer pH 7.5, containing 20 mM HEPES, 100 mM NaCl, 2 mM $MgCl_2$ and 1 mM DTT.

Steady-State Colorimetric dUTPase Assay. Steady-state colorimetric dUTPase assay was performed as described in Pecsi et al.[25] Phenol red indicator assay was used to detect protons released in the dUTPase reaction. $0.1-2$ μM protein in a buffer pH 7.5 was used containing 1 mM HEPES, 100 mM KCl, 40 μM phenol red, and 5 mM $MgCl_2$. A Specord 200 (Analytic Jena, Germany) spectrophotometer and 10 mm path length thermostated cuvettes were used at 20 °C and absorbance was recorded at 559 nm. Initial velocity was determined from the first 10% of the progress curve. The Michaelis—Menten equation was fitted to the steady-state curves.

Enzyme—Ligand Dissociation Constant Measurements. Enzyme—ligand dissociation constant measurements were carried out as circular dichroism intensity titrations. CD spectra were recorded at 20 °C on a JASCO 720 spectropolarimeter using a 10 mm path length cuvette. Protein concentration was 50 μM in a buffer pH 7.5, containing 20 mM HEPES, 50 mM NaCl and 2 mM $MgCl_2$. A spectrum between 250 and 290 nm was recorded at each nucleotide concentration, as described in Pecsi et al.[25] Differential curves were obtained by subtracting the signal of the ligand alone from that of the corresponding complex. Differential ellipticity at 269 nm was plotted against the ligand concentration to obtain the binding curves.

Protein solution was titrated with dUPNPP or dUDP using minute aliquots from a concentrated stock solution. Titration data were fit to the equation describing 1:1 stoichiometry for the dissociation equilibrium with no cooperativity:

$$y = s + \frac{A\left[(c + x + K) - \sqrt{(c + x + K)^2 - 4cx}\right]}{2c}$$

where x is the nucleotide concentration and y is the circular dichroism intensity, $s = y$ at $x = 0$, A is the amplitude of the circular dichroism intensity change, c is the enzyme concentration, and K is the dissociation constant (K_d).

Thermal Stability. Thermal stability measurements were carried out with a JASCO 720 spectropolarimeter using a 1 mm path length cuvette. Wild type and mutants enzymes (25 μM) were measured in a buffer pH 7.5, containing 100 mM NaH_2PO_4 and 2 mM $MgCl_2$. The solution was heated from 20 to 80 °C, and differential ellipticity was recorded by every 0.5 °C at 210 nm. The obtained values were plotted against temperature, and the following Boltzmann curve was fitted:

$$y = A2 + \frac{A1 - A2}{1 + e^{x - x0/dx}}$$

where $A1$ is the initial value and $A2$ is the final value of the differential ellipticity, dx is the time constant, and $x0$ is the inflection point of the curve which is the melting point.

Data Fitting and Statistical Analysis. All experimental measurements were carried out at least three times. Error bars represent standard deviations of the mean of the measurements. Data fitting was performed using Origin 7.5 (OriginLab Corp., Northampton, MA).

Computational Methods. *Structural Model.* The calculations were initiated from the X-ray crystal structures of the wild type and mutant *M. tuberculosis* dUTPase enzymes (Table S1). The original dUPNPP ligand in the crystal structures was manually modified to dUTP. There is a lack of the catalytic water in the T138Stop crystal structure; however, a distinct electron density with a high temperature factor can be seen at the usual position of the attacking water molecule, and this information was used to position a catalytic water molecule into the structure of the T138Stop mutant (Figure S2B). Coordinates of the hydrogen atoms were generated with

CHARMM[37] using standard protonation states of all ionizable residues (also see SI text about potential protonation states of H145). Crystallographic water molecules in the vicinity of the protein and the substrate were preserved while the system has been placed in a cube of TIP3P water to cover at least 10 Å radius in all directions from the protein. Several water molecules were then replaced with a Monte Carlo procedure by ions to account for a 0.10 M NaCl solution, and further Na⁺ ions were added for neutralization.[38] CHARMM27 extended atom force field was used for the molecular mechanics interactions, with periodic boundary conditions, Ewald summation, and a 12 Å cutoff for the evaluation of the nonbonded interactions. After an initial equilibration for 10 ns, with constraints to the initial PDB structure, the final structure was taken as the starting point for subsequent MM and QM/MM minimizations.

QM/MM Setup and Minimizations. The equilibrated classical system was trimmed to a sphere of 21 Å radius centered at the position of the P_α atom of the dUTP, and all residues further than 15 Å were kept fixed. Q-Chem program[39] version 3.1 was used to perform QM calculations, at the B3LYP[40]/6-31+G(d) density functional theory (DFT) level of theory. The quantum mechanical system was coupled with the CHARMM program[37] using full electrostatic embedding.[41] Standard link atom treatment was used to bisect bonds between the QM and MM region, adding hydrogen atoms for the missing ligands. For the QM/MM minimizations, a complex reaction coordinate (Q, Figure 3) was defined as the difference
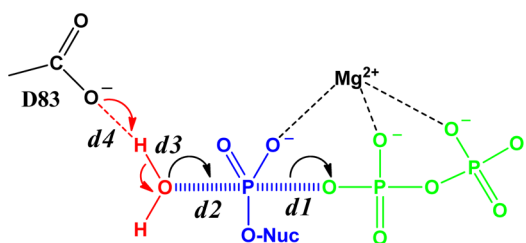

Figure 3. Schematic representation of the reaction coordinate used in the QM/MM simulations. We defined $Q = Q_{ET} + 0.5 Q_{PT}$, where $Q_{ET} = d1 - d2$ denotes the difference between the bond breaking ($d1$) and bond forming ($d2$) distances for the phosphate cleavage (generalized electron transfer coordinate), and $Q_{PT} = d3 - d4$ is the difference between the bond breaking ($d3$) and forming ($d4$) distances for the proton transfer from the water to the Asp83.

between the forming and breaking bond distances in which both phosphate transfer (ET, in analogy with generalized electron transfer) and proton transfer (PT) are incorporated.[42,43] Using this reaction coordinate, the geometries were minimized starting with the initial enzyme–substrate structures and following the reaction through the transition state to the product state. Minimizations were performed using the adopted basis Newton–Raphson scheme as implemented by D. J. States[44] in CHARMM, both in the forward and backward directions to obtain hysteresis-free results.[42]

The quantum region contained the Thr81 and Ile82 backbones, the amide group of Gln113, the side chains of Asp83, Ser65, Thr69 (only in the T138Stop mutant), Ser147 and Ser148 (in the WT and H145A mutant), the side chain of residue 145 (His in the WT, Ala in the H145A mutant), the guanidino group of Arg140 (in the WT and H145A mutant) and Arg64 (only in the T138Stop mutant), the Mg²⁺ ion with its full coordination shell, nearby crystallographic water

molecules, and the dUTP molecule (Figure S1). Thus, the WT, H145A, and T138Stop systems contained 132, 137, and 108 atoms, respectively, in the minimizations with the largest QM region.

After the full QM/MM minimization of the corresponding structures, the charge distribution was analyzed with the Gaussian program package[45] using the CHELPG charge evaluation[46] based on fitting the atomic charges to reproduce the electrostatic potential.[47] In these calculations, the same QM region was used at the same level of theory with an identical polarization scheme as done in the QM/MM minimizations, including the same protein environment in the calculations as external point charges.

QM/MM Dynamics. Short downhill QM/MM dynamics trajectories were generated starting from the minimized WT system near the transition state. The quantum region contained the Thr81 and Ile82 backbones, the amide group of Gln113, the side chains of Asp83, Ser65, His145, Ser147, and Ser148, the guanidino group of Arg140 the Mg²⁺ ion with its full coordination shell, nearby crystallographic water molecules, and the dUTP molecule (121 atoms in total, Figure S1A). We used Langevin dynamics with a friction coefficient of 8 ps⁻¹[48] and an integration time step of 1 fs. During the trajectories, the outer simulation shell was kept fixed as described above. Keeping also the QM region fixed initially, 10 ps long classical MD simulations were carried out first for each downhill trajectory to obtain an ensemble of TS structures with respect to the classical region. These simulations were then followed by unconstrained dynamics using QM/MM calculations with no atoms fixed except for residues further than 15 Å from the P_α atom.

Downhill trajectories were also generated for the T138Stop mutant as described above. The quantum region contained the Thr81 and Ile82 backbones, the amide group of Gln113, the side chains of Asp83, Ser65, Thr69, the Mg²⁺ ion with its full coordination shell, nearby crystallographic water molecules, and the dUTP molecule (95 atoms in total, Figure S1C).

Symmetry Measure Calculations. To analyze the coordination shell of the Mg²⁺ ion, we introduce a continuous, dimensionless symmetry parameter S, similarly to the parameter introduced in Zabrodsky et al.[34] for general geometric structures. Our symmetry measure (S) is defined as

$$S = \min_{\{r,\mathbf{M}\}} \left(\frac{1}{6} \sum_{i=1}^{6} \left| \mathbf{e}_i - \mathbf{M}\left(\frac{\mathbf{x}_i}{r} \right) \right|^2 \right) \tag{1}$$

Here, $\mathbf{x}_i$ are the oxygen position vectors ($i = 1,...,6$) for a given structure, and $\mathbf{e}_i$ are the 6 unit vectors corresponding to the ideal symmetrical octahedral geometry ($\mathbf{e}_1 = (1,0,0)$, $\mathbf{e}_2 = (0,1,0)$, $\mathbf{e}_3 = (0,0,1)$, $\mathbf{e}_4 = (-1,0,0)$, $\mathbf{e}_5 = (0,-1,0)$, and $\mathbf{e}_6 = (0,0,-1)$). For each optimized structure along the reaction profile, we determined S as the minimum distance to an ideal octahedron. This was done by simultaneous optimization of four parameters: (i) the scaling distance r and (ii) the three Euler angles corresponding to the independent elements of the 3D rotation matrix, $\mathbf{M}$. For each optimized structure along the path, we minimized the average distance between the ideal fully symmetric octahedron ($\mathbf{e}_i$) and the rotated, distance scaled, adimensional/dimensionless, octahedron with edges composed of the actual oxygen atom positions of the Mg²⁺ ligands.

■ RESULTS AND DISCUSSION

Steady-State Activities. Steady-state activities of the WT, T138Stop, and H145A mutants were determined by fitting Michaelis−Menten curves to the measured data points (Figure 4). The activity of the H145A mutant decreased by 1 order of
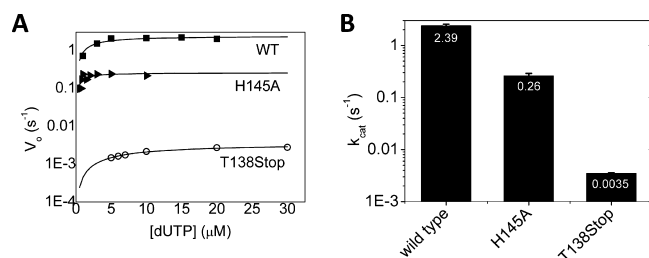

Figure 4. (A) Michaelis−Menten enzymatic activity curves of the wild type and the mutants. (B) Steady-state activity of the dUTPase mutants. Note that both the initial velocity (V_0) and the catalytic rate constant (k_{cat}) values of the mutants are shown on a logarithmic scale.

magnitude, whereas the T138Stop mutant shows 3 orders of magnitude activity decrease. Both values are in agreement with the homologous mutations in the human dUTPase enzyme.[17,25]

Ligand Binding. Ligand binding experiments show that the mutants bind the dUTP analogue α,β-imido-dUTP (dUPNPP) only ∼2−4 times weaker than it does the wild type (Table 1).

Table 1. Measured Kinetic and Ligand Binding Parameters of the Mutants

mutant	WT	H145A	T138Stop
k_{cat} (s^{-1})	3.1 ± 0.06	0.26 ± 0.03	0.0035 ± 0.0001
K_M (μM)	0.46 ± 0.2	0.6 ± 0.2	6.7 ± 0.4
$K_{d\ dUPNPP}$ (μM)	0.9 ± 0.5	2.1 ± 1.0	3.9 ± 1.3
$K_{d\ dUDP}$ (μM)	12.7 ± 3.6	13.6 ± 2.9	13.7 ± 2.3
T_m (°C)	61.2 ± 0.1	58.0 ± 0.4	62.4 ± 0.1

This small change in ligand binding is consistent with the observed structural similarity of the H145A and T138Stop mutants compared to the wild type (see below). We also measured the dUDP binding in the mutant proteins and found no difference compared to the wild type. Because the mutations had some effect on the binding of dUPNPP, but not on the binding of dUDP, the mutated residues thus may promote the selectivity between dUTP and dUDP, as described previously.[17]

No Large-Scale Structural Changes. Thermal stability of the mutants and the wild type has been measured to ensure that the observed differences are not the results of changes in the entire enzyme structure. The measured melting temperatures are similar for both the mutants and the wild type, confirming that the mutations did not induce significant changes in the global protein structure (Table 1).

Crystal Structures. Crystal structures were previously obtained for the H145A[25] and for the T138Stop[15] mutants. These structures demonstrated that the substrate binding is not significantly affected by the mutations and that the overall protein assemblies and substrate binding remained largely similar. The RMSD of the common amino acid atoms with respect to the wild type is 0.12 Å for H145A and 0.20 Å for T138Stop mutant. A smaller but potentially important change in the substrate position was observed for the T138Stop mutant. The substrate gamma phosphate orientation changed

compared to the coordinating Mg^{2+} that is not observed for the H145A (Figure S2A). All other residues remained within 0.5 Å compared to the wild type for both the T138Stop and the H145A mutants.

Structural Changes Compared to the Crystal Structures. There are no significant changes between our structures obtained after minimization and the original crystallographic structures. The overall RMSD of the optimized reactant state (RS) structures and the crystallographic structures are 0.252 Å for the WT, 0.477 Å for the H145A, and 0.336 Å for the T138Stop mutant. The largest deviations are 1.77 Å for the Asp28 O in the case of the H145A mutant and 1.37 Å for the Ser65 O in the case of the T138Stop mutant. These changes are relatively small compared to the crystal structure resolution (1.80 and 1.25 Å for the H145A and T138Stop mutant, respectively), and may also be affected by the presence of the dUPNPP instead of the native dUTP substrate. It is worthwhile to note that both the Asp28 and Ser65 residues are well conserved and found to be important for efficient catalysis.[15,49] An analogous residue to Ser65 has also been found in an alternative conformation in *Bacillus subtilis* dUTPase.[50]

Reaction Mechanism. To investigate the detailed reaction mechanism and the effects of the mutations on the catalytic activity, we performed hybrid QM/MM calculations on the wild type, H145A and T138Stop mutants. Our preliminary minimizations, in which only the phosphate bond forming and breaking coordinates were constrained, confirmed that the proton transfers from the nucleophilic water molecule to the oxygen of the Asp83 carboxylic group. We observed that, when no bias was used on the proton transfer process (i.e., only the Q_{ET} coordinate is biased), as the product was approached, the proton spontaneously transferred to the Asp83. Asp83 is a strictly conserved residue, essential for catalytic activity of trimeric dUTPases. Accordingly, it has been identified in numerous dUTPases as being the universal proton acceptor in the catalytic mechanism.[10,23,51,52] We therefore performed subsequent minimizations along the reaction pathway using the complete reaction coordinate, defined as $Q = d1 − d2 + 0.5(d3 − d4)$ (Figures 3 and 5). Q accounts for all bond breaking and forming processes involved in the rate-limiting catalytic step, including the proton transfer from the nucleophilic water molecule to the acceptor Asp83 residue. For all three obtained pathways, the reaction follows a one-step A_ND_N mechanism regarding the phosphate hydrolysis (Figure S3). The proton transfer from the nucleophilic water to the Asp83 immediately follows the phosphorus bond-forming and bond-breaking steps in a concerted mechanism (Figure 5). The reaction is initiated by the attack of the nucleophilic water, leading to an associative pathway for the phosphate cleavage that has been identified in solution and in several enzymes that carry out phosphate cleavage or transfer (see e.g., Florián et al.[53,54] and Klahn et al.[55]).

This mechanism is also consistent with the experimentally observed pH change that is used to directly follow the reaction kinetics[56] and with the lack of observed intermediates for the phosphate hydrolysis.[33] It is found in *E. coli* dUTPase that two protons transfer to the reaction medium in a concerted mode, immediately following the rate-limiting step.[56] These proton transfer events were also found dependent on two ionizable groups in the protein substrate complex with pK_a values of 5.8 and 10.3.[56] Although the WT and H145A reaction pathways are closely similar to each other, with the H145A pathway being somewhat less concerted (Figures 5 and 6B), a striking
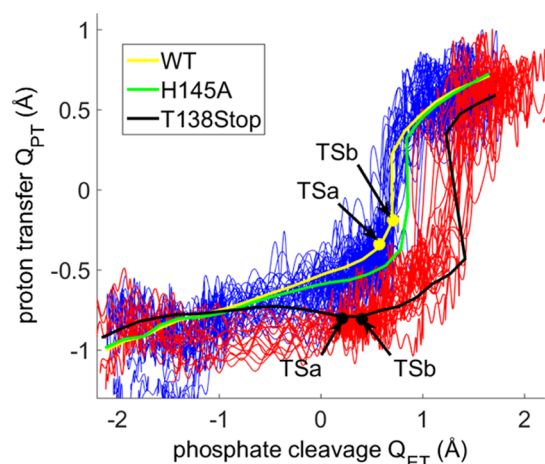
Figure 5. Reaction pathways along the Q_{PT} and Q_{ET} reaction coordinates. Minimum energy pathways are shown for the WT (yellow), H145A (green), and T138Stop (black) systems. Unbiased downhill QM/MM MD trajectories are also shown for the WT (blue) enzyme and for the T138Stop (red) mutant. The downhill trajectories (thin lines) were initiated from near the corresponding transition state (TS) positions for each system (arrows and symbols). TSa and TSb correspond to the nearest points to the transition state on the reactant and on the product side along the minimized pathways, respectively (see the Downhill Trajectories section for further details).

difference is observed for the T138Stop mutant. For this enzyme, which lacks the C-terminal arm, we observed a much more stepwise reaction profile (Figures 5 and 6), with the proton transfer being decoupled from the phosphate cleavage. A comparison of the bond-forming and -breaking distances (Figure 6B) reveals that the crossing points of equal P−O distances happen the earliest for the T138Stop mutant, followed by the H145A and the WT enzymes along the reaction coordinate Q. Accordingly, the crossing point for the O−H distances is located along Q first for the WT enzyme, followed closely by the H145A, and finally it takes place at the largest Q value for the T138Stop system. We find consistently that the extent of concertedness of the proton transfer (PT) correlates with the calculated energy barrier, and the experimental activity (cf. also Tables 1, 2).

The reaction energies (Table 2 and Figure 6A) are in very good qualitative agreement with the experimental catalytic rates, particularly the observed trend of decreased catalytic activities of T138Stop with respect to WT and H145A. The calculated activation energies are shown in Table 2, together with the activation Gibbs free energies which were obtained from the measured catalytic rate constants using a 6.1×10^{12} s^{-1} prefactor. The energy barrier for the WT enzyme is in excellent quantitative agreement with the derived experimental activation free energy. The order of activities among the three enzymes is also properly predicted. The calculated barriers are higher for the H145A and T138Stop mutants than the experimentally observed ones; however, their relative activities are recovered consistently. In the future, more computationally demanding free-energy calculations with extensive sampling could be used to account quantitatively for the energy profiles evidenced in this study.

Transition States Geometries and Electronic Structure. To characterize the transition states, we have analyzed the geometrical parameters corresponding to the bonds breaking and forming during the phosphate cleavage and the proton
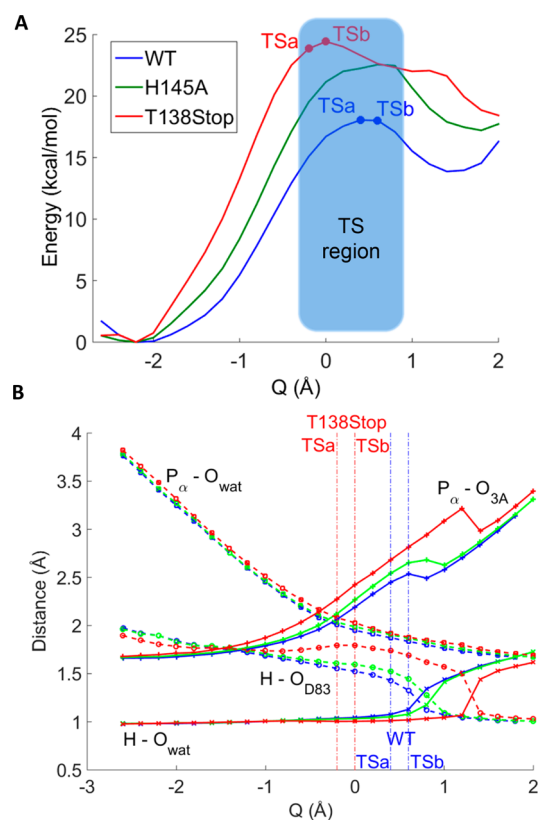

Figure 6. (A) Energy profiles for the catalytic reaction and (B) distances of the forming ($P_{\alpha}-O_{wat}$, dashed lines and squares), breaking ($P_{\alpha}-O_{3A}$, solid lines and + symbols), forming H−O_{D83} (dashed lines and circles), and breaking open H−O_{wat} (solid lines and x symbols) bonds along the reaction coordinate Q. WT, H145A and T138Stop systems are shown with blue, green and red, respectively. TS region is highlighted for WT and T138Stop. TSa and TSb (vertical dash-dot lines) correspond to adjacent points at the TS along the optimized pathways, at the reactant and product side, respectively (see the Downhill Trajectories section for further details).

Table 2. Measured Activation Free Energies and Calculated Activation Energies (kcal/mol)

	measured $\Delta G^{\ddagger}$	calcd $\Delta E^{\ddagger}$
wild type	16.6	18.0
H145A	17.9	22.6
T138Stop	20.4	24.4

transfer processes (Table S2). In all three systems, the transition state corresponds to long $P_{\alpha}-O_{3A}$ leaving group distances, viz., in the range of 2.3−2.6 Å, where the $P_{\alpha}-O_{3A}$ bond is already broken. These late-transition-state structures thus have a dissociative character and fit well into the loose transition states extensively described in previous experimental studies, based on oxygen kinetic isotope effect data and the slopes of Brønsted plots in linear free energy relationships for analogous phosphate cleavage reactions in enzymes and in solution.[57−60] Interestingly, the $O_{wat}-P_{\alpha}$ bond length shows greater variations at the TS for the three enzymes; it is the shortest for the WT and the longest for the T138Stop mutant. Overall, the WT enzyme presents the most "loose" transition state geometry, whereas the almost inactive T138Stop enzyme has the most compact transition state.

To further compare the bonding patterns at the transition states of the three different systems, we also performed Natural

Bond Orbital (NBO) analysis at the respective transition state geometries. Consistent with the coupled proton transfer pathway (Figure 5), the bonding analysis reveals simultaneous occurrence of the following events: bond forming between the O_{wat}–P_α atoms, bond breaking at the O_{wat}–H_{wat} bond, and formation of the new O_{D83}–H_{wat} bond (Figure 7, top). The two
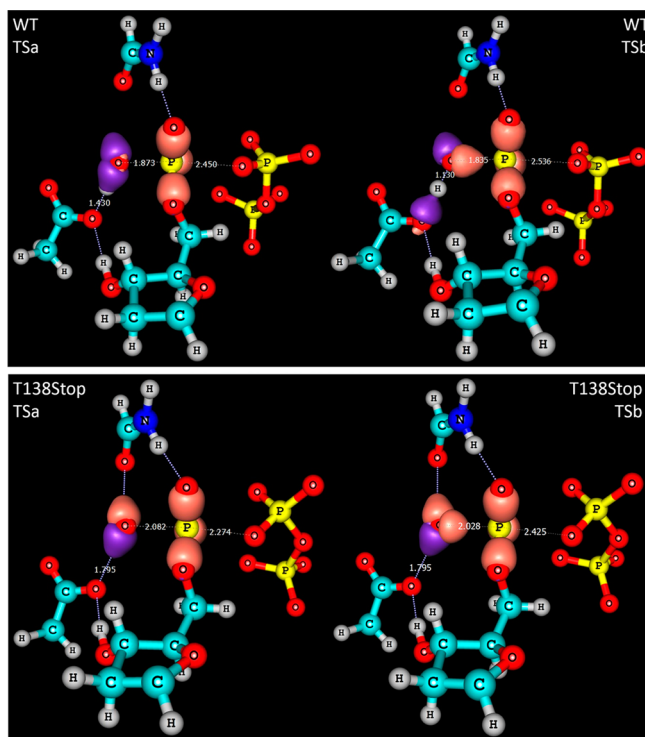

Figure 7. NBO analysis of the transition state structures in the WT and T138Stop enzymes. The molecular orbitals at the 0.2 au electron density level are shown for all natural bonds of only the H_{wat}, O_{wat}, and P_α atoms. For clarity, only part of the QM region corresponding to the deoxyribose triphosphate, the nucleophilic water, the proton accepting Asp83 side chain and the Thr81 and Ile82 backbones are shown.

structures at the barrier top correspond to the changing bonding pattern with respect to these three bonds, highlighting all the bonds formed by the H_{wat}, O_{wat}, and P_α atoms in each case. The H145A enzyme has a more flat transition state region, with already formed O_{wat}–P_α bond at the $Q = 0.2$ Å and $Q = 0.8$ Å regions (Figure S4). The energy then finally drops corresponding to the deprotonation of the water at larger reaction coordinate values (Figure 6A). The proton transfer and the phosphate cleavage are the most decoupled for the T138Stop enzyme, where the transition state corresponds only to the formation of the O_{wat}–P_α bond (Figure 7, bottom). The NBO analysis provides a consistent picture clarifying the nature of the chemical bonding at the transition states in all three systems. We find that the P_α–O_{3A} bond between the leaving group and the phosphorus is broken in all three cases, presenting a concerted mechanism with a loose dissociative TS. The NBO analysis also confirms the simultaneous bond formation of the new O_{wat}–P_α bond and the proton transfer from the water to the Asp83 for the WT system, whereas the transition state corresponds to the formation of the new O_{wat}–P_α bond only in the T138Stop enzyme, and the proton transfer follows subsequently.

Solvent Kinetic Isotope Effects. To determine the involvement of the proton transfer in the catalytic reactions, we carried out frequency calculations at the reactant and transition states using the QM/MM optimized geometries of the reaction pathways. The MM atoms were considered as point charges only, and therefore, the additional imaginary frequencies corresponding to the approximate Hessian were excluded.[61] These frequencies were consistently the same both for the RS and TS geometries, whereas additional imaginary frequencies with the larger intensity peaks were present in the TS structures only. The vibrational motion of these TS frequencies corresponded to the bond breaking and forming coordinates. We estimated the solvent kinetic isotope effects (solvent KIEs) by performing calculations using standard proton mass as well as using deuterated water molecules. On the basis of the estimated free energy difference ($\Delta\Delta G^\ddagger$) between the calculated zero-point vibrational energies for the D_2O/H_2O systems at the TS/RS, we obtained the solvent kinetic isotope effects of about 1.8 to 3.2 for the WT (corresponding to the TSa: $Q = 0.4$ Å and TSb: $Q = 0.6$ Å structures, respectively), 1.4 to 2.2 for the H145A (corresponding to the optimized structures within the range of $Q = 0.2$ to 0.8 Å), and 1.01−1.02 for the T138Stop systems (corresponding to TSb: $Q = 0.0$ Å and TSa: $Q = −0.2$ Å structures, respectively). The results suggest the loss of solvent KIEs for the nearly inactive T138Stop mutant.

Downhill Trajectories. As an additional test of the mechanistic reaction pathway found with QM/MM minimizations, we ran sets of downhill QM/MM trajectories. Geometry optimizations in proteins are well-known to suffer from being trapped in some of the myriads of local minima, and free energy calculations are necessary for more quantitative results.[62,63] Here we tested whether our minimized pathways correspond to the ones obtained by dynamical trajectories. We initiated random downhill trajectories from near the transition states for the WT enzyme and the T138Stop mutant, starting from different thermally equilibrated classical regions. The obtained trajectories initiated at conformations close to the transition state (Figure 6) indeed terminated both at the reactant side and the product side, confirming that the starting structures were part of the TS ensemble.

For the WT system, a total of 86 simulations were initiated from the QM/MM optimized structures at the $Q = 0.4$ Å (66 trajectories, all 100 fs long), and $Q = 0.6$ Å (20 trajectories of length between 317 and 584 fs) values of the reaction coordinate (Figure 5, TSa and TSb, respectively). Out of the 66 trajectories initiated at $Q = 0.4$ Å (closer to the reactants, TSa), 4 remained near the transition state, 14 reached the product state, and 48 the reactant state. Out of the 20 trajectories, initiated at $Q = 0.6$ Å (closer to product, TSb), 12 reached the product state, and 8 the reactant state.

For the T138Stop system, 20 trajectories were initiated both at $Q = −0.2$ Å (Figure 5, TSa), and also at $Q = 0.0$ Å, at the free energy barrier maximum (Figure 5, TSb). Trajectories were run between 70 and 1000 fs long, each dynamics reaching reaction coordinate values either below $Q = −1.47$ Å (RS) or above $Q = 1.61$ Å (PS). Fourteen out of the 20 trajectories reached the product state, and 6 the reactant state starting from $Q = 0.0$ Å, and 12 reached the reactant state, 8 the product state starting at $Q = −0.2$ Å. Note that we have carried out both forward and backward minimizations using our complex reaction coordinate to avoid hysteresis as much as possible.[42]
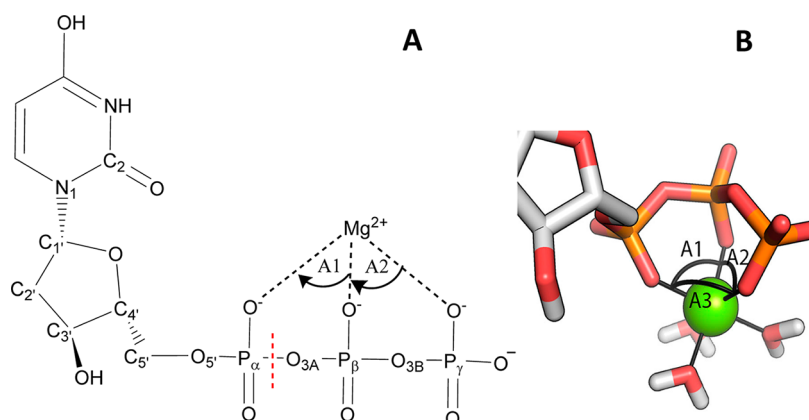
Figure 8. (A) Schematic view of the dUTP molecule coordinated to the Mg^{2+} ion. (B) The hexacoordinated Mg^{2+} ion, as bound in the active site. Definition of the three angles, A1, A2, and A3, are also shown.

Note also that the downhill reaction pathways for WT and T138Stop are initiated near the maxima of the corresponding energy profiles. These positions, do not necessarily have to coincide with the actual TS locations (i.e., having a splitting probability of 0.5) along the reaction coordinate Q,[64] though in this case they are clearly very close.

We obtained a very good correlation between the reaction pathway calculated by QM/MM minimizations and the ensemble of pathways obtained via downhill trajectories (Figure 5). We could also confirm the distinct difference between the reaction pathways for the WT and T138Stop enzymes, with the latter being much more stepwise.

Mg^{2+}-Ion Coordination. Mg^{2+} is an essential cofactor in most phosphoryl transfer and hydrolysis catalyzing enzymes. Its role in modulating the catalytic reaction, however, is not yet well understood. We investigated the Mg^{2+} coordination, in particular, focusing on the O—Mg—O angles during the reaction (Figures 8 and S5). Three angles, labeled A1, A2, and A3 (Figure 8B), are most relevant to characterizing the phosphate—magnesium binding geometry: (i) A1, between the α- and β-phosphates and the Mg^{2+} (O1A—Mg—O1B); (ii) A2, between the β- and γ-phosphates and the Mg^{2+} (O1B—Mg—O2G); and (iii) A3, between the α- and γ-phosphates and the Mg^{2+} (O1A—Mg—O2G). The increase in A1 and A2 (Figure S5) correlates strongly with the changes in the reaction coordinate, whereas A3 changes only in case of the T138Stop mutant. A1 and A2 reach the ideal 90° angle—required for the symmetric octahedral Mg^{2+} coordination—right before the transition state region of the reaction pathway. A3, on the other hand, remains at around 100° throughout the reaction profile for the WT and H145A enzymes (Figure S5), thus causing a small distortion from an ideal octahedral Mg-coordination. The γ-phosphate in the T138Stop mutant is not coordinated by key protein residues observed in the WT, due to the lack of the C-terminal arm. Accordingly, as compared with the wild type, the Mg^{2+} coordination in this mutant leads to the largest differences in the values of A3 (Figure S5), an angle involving the γ-phosphate.

Continuous Symmetry Measure. To provide a generic, quantitative analysis tool measuring the changes in the Mg^{2+} coordination (i.e., the symmetry) along the reaction profile, we implemented a simple algorithm to calculate a continuous symmetry measure[34] around the Mg^{2+}. We use this symmetry measure S (see eq 1) to follow the changes along catalytic reactions. Previously, symmetry measures have been applied to

a variety of systems, such as studies of interconversion paths in transition metal chemistry.[65−67] We determined the overall coordination symmetry in the three different systems using the continuous symmetry measure S (Figure 9). Interestingly, all
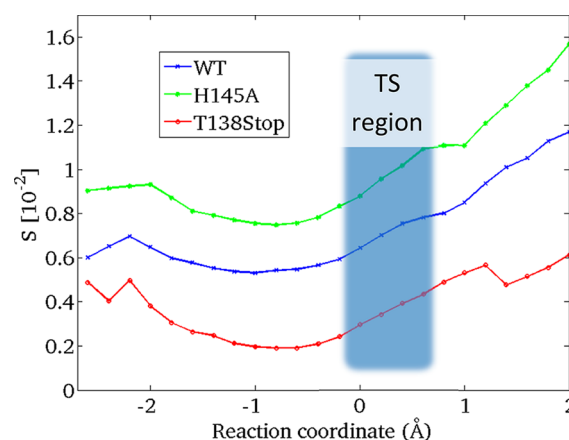

Figure 9. Symmetry parameter (S) along the reaction profile. Mg^{2+} coordination becomes most symmetric (i.e., smaller S values) before the transition state region (TS, blue area) is reached. A more symmetrical Mg^{2+}-coordination could drive the reaction toward the TS region. S is defined according to eq 1.

systems display the same general trend: the coordination becomes gradually more symmetrical as the reaction progresses, and a minimum in S is reached before the transition state. After this point, the symmetry measure S increases again, as the product state is reached. Interestingly, the T138Stop mutant has the most relaxed and symmetrical Mg^{2+} coordination compared with the WT and H145A, due to the lack of the C-terminal arm, which would coordinate the phosphate chain of dUTP (Figure 9). Reaching more symmetrical coordination around the Mg^{2+} should energetically stabilize the TS compared with the reactant state (RS), and the lack of this difference in the stabilization between RS and TS may lead to decreased activity. In general, however, it is hard to quantify the energetic contribution arising due only to the changes in the Mg^{2+}-coordination. Based on thorough gas-phase and solution studies by the Florián group,[68] analyzing the energetics of distortions in metal ion coordination, the energetic stabilization may be estimated on the order of 2 kcal/mol. To sum up, the Mg^{2+}-coordination symmetry varies along the reaction coordinate
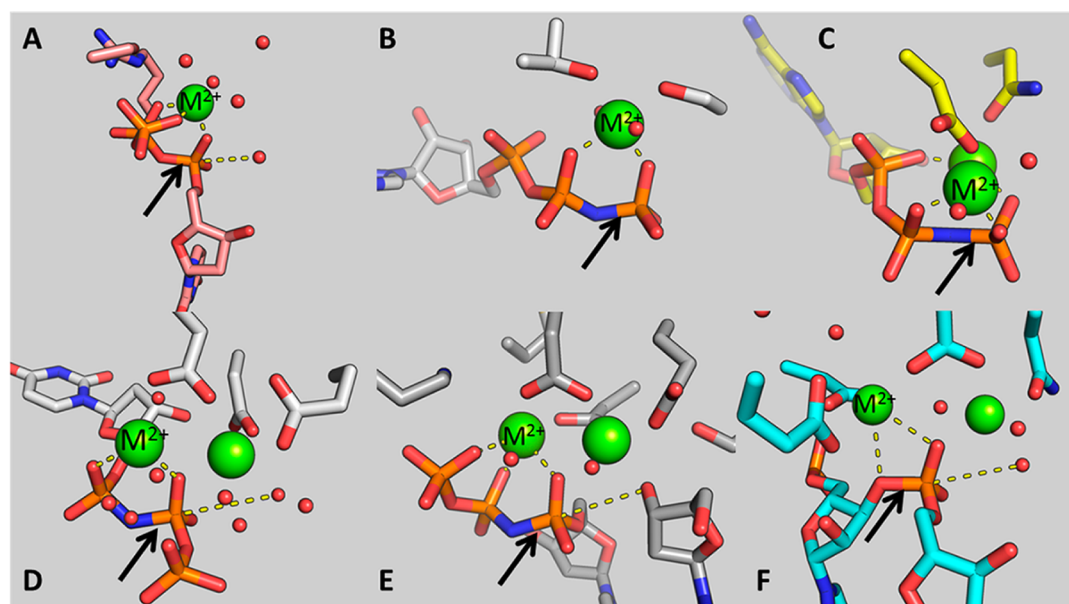
Figure 10. Equivalent active-site metal ion (M^{2+}) positions in various phosphate processing enzymes. The residues within 4 Å around the metal ions (green spheres) are shown as sticks. Prototype Mg^{2+} coordination geometries are presented for trimeric dUTPases (A, PDB ID: 2PY4), ATPases (B, PDB ID: 3ZFD), Ser/Thr kinases (C, PDB ID: 4DFX), dimeric dUTPases (D, PDB ID: 2CIC), polymerases (E, PDB ID: 4Q8E), and RNases H (F, PDB ID: 1ZBL). The scissile P−O bonds (or its nonhydrolyzable equivalents) are highlighted by arrows.

consistently in all our three systems, and thus, the metal coordination symmetry emerges as a possible contributing factor to the catalytic mechanism.

Role of the C-Terminal Arm in Substrate Specificity. Interestingly, the particularly important role of the A2 and A3 angles involving the γ-phosphate (Figure 8B) could contribute to the dUDP/dUTP specificity via the C-terminal arm, preventing the dUDP hydrolysis while allowing it for dUTP. For *E. coli* enzymes, it was found that the flexible C-terminal arm takes up an ordered structure only in the presence of the γ-phosphate,[29,30] whereas other organisms such as the human dUTPase may have a C-terminal arm located in the vicinity of the active site, even when a bound substrate is absent.[69] A recent mutational study demonstrated that the C-terminal arm P-loop-like motif is required for catalytic activity and it also helps to discriminate against dUDP substrates.[17] The differences we observed in angles A2 and A3 along the catalytic reaction (Figure S5) with the C-terminal arm present (WT and H145A) and absent (T138Stop) are also consistent with distinct changes in the dihedral angles of the triphosphate chain. Three relevant dihedral angles of the triphosphate backbone, $O_{5'}$−P_α−O_{3A}−P_β (A), P_α−O_{3A}−P_β−O_{3B} (B), and O_{3A}−P_β−O_{3B}−P_γ (C) (Figure S6), show a distinctly different orientation of the chain for the T138Stop mutant as compared to the WT and H145A. The same trend is also observed in the original crystallographic structures with nonhydrolyzable ligands (Table S1 and Figure S2A). This may offer new mechanistic insights about the role of the C-terminal arm structural motif in the dUDP/dUTP specificity.

Analogy with Two-Metal Ion Catalysis. In many enzymes that carry out phosphoryl transfer and hydrolysis, the reacting phosphate groups are coordinated via divalent metal ions, in the active site, mainly Mg^{2+} (Figure 10). A common ubiquitous two-metal ion catalytic mechanism was proposed for polymerases and nucleases by Steitz and Steitz.[70] In this mechanism, metal ion A coordinates the nucleophile, whereas metal ion B coordinates the leaving group. Similar to

dUTPases, only a single metal ion is involved in the catalytic reaction of several enzymes, such as nucleases with the ββα-Me structural motifs,[71,72] or HUH motifs (where H's denote two histidine residues separated by a hydrophobic residue, U).[69,73,74] An analogous role of the single metal ion in one-metal ion catalysis has been proposed to metal ion B in two-metal ion catalysis based on structural data.[8] An additional emerging role for metal ion B is to take on a more symmetrical coordination near the transition state region and thereby to facilitate catalysis.[8,43] These roles show great similarities to the roles of metal ion B in two-metal ion catalysis.[43]

An analogous metal ion is also present in most AAA+ ATPases coordinating the ATP at the β- and γ-phosphates, but not the α-phosphates (Figure 10B). Related phosphate transfer reactions are carried out by kinases cleaving ATP and transferring the γ-phosphate to an alcohol group of an amino acid side chain (typically Ser, Thr, or Tyr). In this important family of enzymes, two Mg^{2+} ions are commonly observed in high-resolution crystal structures, with a consensus structure for Ser/Thr kinases where one of the metal ions coordinates α-, β-, and the γ-phosphates, whereas the second metal ion coordinates β- and γ-phosphates, as in for example cyclic AMP-dependent protein kinase (PKA, Figure 10C).[75] Intriguingly, both metal ions coordinate the cleaved γ-phosphate of the ATP for these catalytic reactions, whereas none coordinate the attacking oxygen nucleophile in these highly specific enzymes, just as in dUTPases. The role of the two metal ions in these kinases therefore resembles the role of metal ion B in two-metal ion catalysis, and the single metal ion observed in one-metal ion catalysis in ATPases and dUTPase. Interestingly, the Mg^{2+} to Ca^{2+} substitution effects are typically also similarly inhibitory[76] for two-metal ion catalysis as well as for the one-metal ion catalysis in dUTPase[21,22] and in several ATPases[77−81] and kinases,[78,82,83] with some notable exceptions.[84,85]

This key metal ion often coordinates the cleaved phosphate. This helps the catalysis by lowering the pK_a of the phosphate group. As the overall effect of this Mg^{2+} coordination, the α-
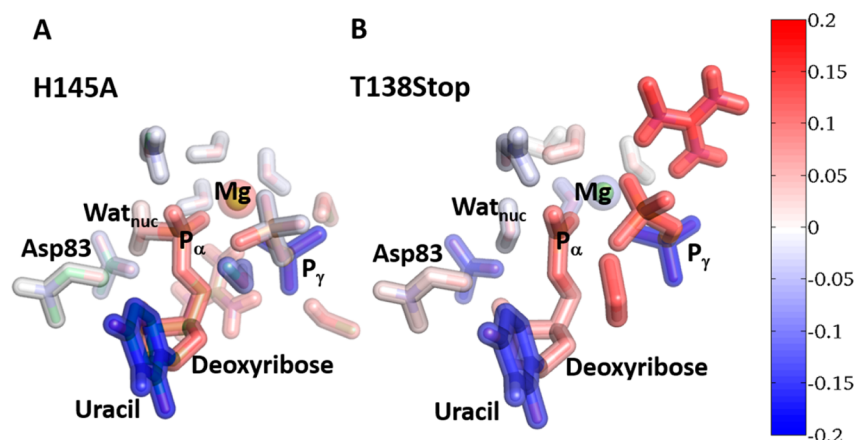
Figure 11. Charge distribution difference for the QM region of (A) H145A and (B) T138Stop mutants compared with the WT enzyme, using the CHELPG atomic charge scheme as implemented in Gaussian09. The atoms are displayed in solid sticks using a color scheme based on the elements and with wider transparent sticks using a blue−white−red color scheme, in the range of −0.2 e to +0.2 e (scale bar in atomic units), based on the charge difference for the group of atoms between the (A) H145A or (B) T138Stop simulation and the WT. For definition of the atomic groups and the numerical values for the charge differences, see Table S3.

phosphate oxygen atoms are more acidic, and thus their protonation is significantly less favorable. Accordingly, the single most likely proton transfer pathway corresponds to the protonation of the Asp83, and protonation of the α-phosphate is unfavorable.

The prominent role of the Mg^{2+} ion in lowering of the pK_a of its ligands is also important for the second ion in two-metal ion catalysis. In this case, the second Mg^{2+} ion typically coordinates the nucleophilic water (or the attacking group, in general). This was observed to lead to a mechanism with early proton transfer, preceding the coupled phosphate cleavage in the RNase H catalytic reaction.[43,76] Likewise, early proton transfer was found to take place in the two-metal ion-catalyzed reactions of DNA polymerases[86] and adenylyl cyclases.[87] In one-metal ion catalysis, the unligated nucleophilic water has a higher pK_a, which explains the difference in the mechanism leading to the late proton transfer observed in this study as well.

A key consensus role thus emerges for a functional Mg^{2+} ion that coordinates the cleaved phosphate. The specific active site geometry and fine-tuning of the pK_a-s of the catalytic groups by the metal ion leads to a reaction mechanism that is very different from the corresponding slow, uncatalyzed reaction in water.[88,89] Thus, the Mg^{2+} ion appears to have an essential contribution for the highly specific catalytic reactions, by (i) lowering the pK_a of the leaving group, and by (ii) imposing a specific constrained geometry for the triphosphate chain, which drives the reaction toward its transition state and products.

Conserved π−π Stacking Interaction with the NTP Nucleobase. Despite the relatively large (∼7 Å) distance of the H145 residue from the P_α cleavage site, this residue has a significant contribution to the catalytic activity. It establishes a π−π stacking interaction with the uracil ring (Figure 1B),[25] taking up a T-shaped orientation of the rings.[90] This well-conserved interaction is also observed in many other trinucleotide-binding enzymes, including ABC transporters,[91] kinesins,[92] or kinases.[93] The general importance of aromatic residues corresponding to the H145 amino acid across many dUTPases was established in a study of 500 dUTPase sequences.[25] Among these 500 structures, the most conserved residue is Phe (96.4% of cases), whereas His accounted for 1.8% of the structures. Based on our measurements and on the kinetic measurements reported,[25] the catalytic rate was affected

when the aromatic residue was mutated to an Ala, whereas the substrate binding remained relatively intact as compared to the wild type. The loss of catalytic activity was about 10 to 20-fold,[25] both in the human and in the *M. tuberculosis* enzymes. There is thus an outstanding puzzling question as to how the conserved π−π stacking interaction affects the catalytic reaction, from such a remote distance to the cleavage site.

Charge Distribution of the QM Regions at the TS. T-shaped π−π stacking interactions are thought to have more electrostatic character compared with sandwich-shaped orientations.[94] To better understand whether the π−π stacking interactions with the nucleobase may produce additional charge transfer that in turn would promote catalysis, we calculated the partial charges for the minimized structures. We compared the charge distribution in the WT with the mutants, in their respective TS conformations. It is important to emphasize that the charge distribution of the high energy TS is the main determining factor of the catalytic barrier, whereas the charge distribution at the RS is less relevant for predicting reactivity. For both mutants, we calculated the difference in the distribution of partial charges, as illustrated in Figure 11 using a color coding where blue means that the group is more negative than the WT, red means that the group is more positive, and white means no change in overall charge. The color code ranges between −0.2 and 0.2 e. The numerical values are also given in Table S3.

We observed that the uracil ring has a significantly altered polarization due to the missing π−π stacking interaction, and this also affects the sugar moiety (Figure 11 and Table S3). However, the geometric differences corresponding to the H145A mutation are likely the main reason for the decreased activity of the H145A mutant (SI text).

Intriguingly, both mutants have similar changes in the polarization of the active site at the TS geometries. We find that the largest change is observed in the polarization of the relatively distant γ-phosphate, interestingly, which becomes more negative at the H145A and T138Stop enzymes compared to the WT TS. Likewise, the uracil group also becomes more negative at the TS in the H145A and T138Stop mutants compared with the WT, whereas the deoxyribose and the α-phosphate groups have a more positive partial charge in the mutant enzymes.

CONCLUSIONS

Phosphate cleavage and transfer reactions are universal in all biological processes of all living organisms. Furthermore, phosphate-based reaction mechanisms have many common aspects shared among the majority of enzymes that carry out the corresponding catalytic reactions, such as the use of divalent Mg^{2+} ions.[35]

We investigated here the phosphate cleavage reaction in the WT and two mutant forms (H145A and T138Stop) of dUTPase enzyme complexes. Our analysis of steady-state activities of the WT and T138Stop and H145A mutants showed that the activity of the H145A mutant is lower by 1 order of magnitude, while that of the T138Stop mutant is lower by 3 orders of magnitude, as compared to the WT, in agreement with the homologous mutation in the human dUTPase enzyme.[17] To understand what the key factors are that might control the observed changes in the catalytic activities, we studied the reaction mechanism of proton transfer and phosphate cleavage using QM/MM methodology. We found a one-step associative A_ND_N pathway for the catalytic mechanism with a loose dissociative TS in all three systems. The dUTPase hydrolysis of the α-phosphate also involves a coupled proton transfer from the nucleophilic water to the catalytic Asp83 residue. The coupled proton transfer occurred in a single step with the phosphate cleavage in the following sequence of events. First, the nucleophilic water approached the phosphate. Subsequently, the $P_\alpha-O_{3A}$ bond broke. At the TS in the WT enzyme, the new $P_\alpha-O_{wat}$ bond formed at the same time as the proton transfer from the water to the Asp83 was initiated. The final products were then reached by completing the proton transfer. Essentially, we observed the same mechanism taking place in all the three systems. The main difference was that the proton transfer was decoupled from the TS in the two mutants as confirmed by NBO analysis, and it happened particularly late in the nearly inactive T138Stop mutant. We did not observe major differences in the ligand binding, protein stability, or in the structures of the assembled complexes. However, the degree of concertedness of the proton transfer and the phosphate bond formation at the TS were correlated strongly with the known catalytic activities. We observed less concerted proton transfer in case of the H145A mutant and further significantly decreased concertedness for the T138Stop mutant. Our calculations also suggest the loss of solvent KIEs for the T138Stop mutant. Our calculated reaction barriers are also in agreement with the catalytic rates measured in our corresponding site-directed mutagenesis experiments. The observed concerted coupled proton transfer appears to be a general mechanism in enzymes that catalyzes phosphate transfer and cleavage reactions.[43,76,95−98]

Our calculations also provided evidence that the specific metal ion coordination mode may play a prominent role in the catalytic reaction. We developed a new implementation to quantitatively determine the symmetry around the metal ion during the catalytic reaction. Based on our analysis using the calculated continuous symmetry measure[34] of the metal ion coordination throughout the reaction, a symmetric, octahedral Mg^{2+} coordination was shown to stabilize the TS for all cases. All three systems displayed the same trend for the change in the metal-coordination symmetry along the reaction pathway. The T138Stop mutant had the most symmetrical and thus the most relaxed coordination around the Mg^{2+} throughout the reaction, due to the lack of the C-terminal arm. Changes in the charge distributions of the three systems in their respective TS, also revealed significant differences in the partial charge transfer from the protein to the substrate, due to the missing native protein−protein and protein−substrate interactions in the mutants. The uracil group has a larger partial negative charge in the mutant structures at the TS compared to the WT, whereas deoxyribose is more positively polarized. Interestingly, the negative polarization of the γ-phosphate is the largest change between the partial charges of the TS structures. Geometrical relaxation of the active site due to mutations could play a key role in altering the TS-s, leading to a more decoupled proton transfer. The key emerging roles for a functional Mg^{2+} ion that coordinates the phosphate leaving group are (i) to lower the pK_a of the cleaved phosphate groups and (ii) to impose constrained coordination geometry on the Mg^{2+}, which drives the reaction toward the transition state and product.

The structural and electronic changes involved in the dUTPase catalytic reaction evidenced here, in conjunction with the experimental data, shed new light on the crucial role of the dUTPase C-terminal arm in modulating ligand binding geometry and catalytic activity and of the essential roles of the Mg^{2+} ion cofactor. Detailed understanding of the reaction process provided by this study could lead to the design of new drugs and new approaches to rationally control the activity of dUTPase and other (e.g., ATPase, kinase or polymerase) enzymes.

ASSOCIATED CONTENT

Ⓢ Supporting Information

The following file is available free of charge on the ACS Publications website at DOI: 10.1021/cs502087f.

> Supporting Information consists of six additional figures (Figures S1−S6), three tables of data (Tables S1−S3), and two paragraphs on the protonation state of H145 and on the structural and polarization effect of the H145A mutation (PDF)

AUTHOR INFORMATION

Corresponding Authors
*E-mail: tothj@enzim.hu.
*E-mail: Vertessy.Beata@ttk.mta.hu.
*E-mail: Edina.Rosta@kcl.ac.uk.

Present Addresses
¶(A.L.) Laboratory of Molecular Physiology, National Heart, Lung, and Blood Institute, National Institutes of Health, Bethesda, MD 20892, U.S.A. and Astbury Centre for Structural Molecular Biology, Faculty of Biological Sciences, University of Leeds, Leeds, LS2 9JT, U.K.
#(P.K.S.) Department of Chemistry, Cotton College State University, Guwahati 781001, India.

Notes
The authors declare no competing financial interest.

ACKNOWLEDGMENTS

■ REFERENCES

(1) McIntosh, E. M.; Ager, D. D.; Gadsden, M. H.; Haynes, R. H. *Proc. Natl. Acad. Sci. U. S. A.* **1992**, *89*, 8020−8024.

(2) Björnberg, O.; Neuhard, J.; Nyman, P. O. *J. Biol. Chem.* **2003**, *278*, 20667−20672.

(3) Johansson, E.; Björnberg, O.; Nyman, P. O.; Larsen, S. *J. Biol. Chem.* **2003**, *278*, 27916−27922.

(4) Huffman, J. L.; Li, H.; White, R. H.; Tainer, J. A. *J. Mol. Biol.* **2003**, *331*, 885−896.

(5) Li, H.; Xu, H.; Graham, D. E.; White, R. H. *J. Biol. Chem.* **2003**, *278*, 11100−11106.

(6) Helt, S. S.; Thymark, M.; Harris, P.; Aagaard, C.; Dietrich, J.; Larsen, S.; Willemoes, M. *J. Mol. Biol.* **2008**, *376*, 554−569.

(7) Vertessy, B. G.; Toth, J. *Acc. Chem. Res.* **2009**, *42*, 97−106.

(8) Yang, W. *Nat. Struct. Mol. Biol.* **2008**, *15*, 1228−1231.

(9) Mustafi, D.; Bekesi, A.; Vertessy, B. G.; Makinen, M. W. *Proc. Natl. Acad. Sci. U. S. A.* **2003**, *100*, 5670−5.

(10) Chan, S.; Segelke, B.; Lekin, T.; Krupka, H.; Cho, U. S.; Kim, M.-y.; So, M.; Kim, C.-Y.; Naranjo, C. M.; Rogers, Y. C.; Park, M. S.; Waldo, G. S.; Pashkov, I.; Cascio, D.; Perry, J. L.; Sawaya, M. R. *J. Mol. Biol.* **2004**, *341*, 503−517.

(11) Tarbouriech, N.; Buisson, M.; Seigneurin, J.-M.; Cusack, S.; Burmeister, W. P. *Structure* **2005**, *13*, 1299−1310.

(12) Camacho, A.; Arrebola, R.; Pena-Diaz, J.; Ruiz-Perez, L. M.; Gonzalez-Pacanowska, D. *Biochem. J.* **1997**, *325* (Pt 2), 441−447.

(13) Moroz, O. V.; Harkiolaki, M.; Galperin, M. Y.; Vagin, A. A.; Gonzalez-Pacanowska, D.; Wilson, K. S. *J. Mol. Biol.* **2004**, *342*, 1583−97.

(14) Hemsworth, G. R.; Moroz, O. V.; Fogg, M. J.; Scott, B.; Bosch-Navarrete, C.; Gonzalez-Pacanowska, D.; Wilson, K. S. *J. Biol. Chem.* **2011**, *286*, 16470−81.

(15) Takacs, E.; Nagy, G.; Leveles, I.; Harmat, V.; Lopata, A.; Toth, J.; Vertessy, B. G. *FEBS Lett.* **2010**, *584*, 3047−54.

(16) Fiser, A.; Vertessy, B. G. *Biochem. Biophys. Res. Commun.* **2000**, *279*, 534−42.

(17) Pécsi, I.; Szabó, J. E.; Adams, S. D.; Simon, I.; Sellers, J. R.; Vértessy, B. G.; Tóth, J. *Proc. Natl. Acad. Sci. U. S. A.* **2011**, *108*, 14437−14442.

(18) Walker, J. E.; Saraste, M.; Runswick, M. J.; Gay, N. J. *EMBO J.* **1982**, *1*, 945−951.

(19) Ogura, T.; Wilkinson, A. J. *Genes Cells* **2001**, *6*, 575−597.

(20) Hanson, P. I.; Whiteheart, S. W. *Nat. Rev. Mol. Cell Biol.* **2005**, *6*, 519−529.

(21) Hidalgo-Zarco, F.; Camacho, A. G.; Bernier-Villamor, V.; Nord, J.; Ruiz-Perez, L. M.; Gonzalez-Pacanowska, D. *Protein Sci.* **2001**, *10*, 1426−33.

(22) Persson, R.; McGeehan, J.; Wilson, K. S. *Protein Expression Purif.* **2005**, *42*, 92−9.

(23) Harris, J. M.; McIntosh, E. M.; Muscat, G. E. O. *J. Mol. Biol.* **1999**, *288*, 275−287.

(24) Warshel, A.; Levitt, M. *J. Mol. Biol.* **1976**, *103*, 227−249.

(25) Pecsi, I.; Leveles, I.; Harmat, V.; Vertessy, B. G.; Toth, J. *Nucleic Acids Res.* **2010**, *38*, 7179−86.

(26) Varga, B.; Barabas, O.; Takacs, E.; Nagy, N.; Nagy, P.; Vertessy, B. G. *Biochem. Biophys. Res. Commun.* **2008**, *373*, 8−13.

(27) Mol, C. D.; Harris, J. M.; McIntosh, E. M.; Tainer, J. A. *Structure* **1996**, *4*, 1077−92.

(28) Shao, H.; Robek, M. D.; Threadgill, D. S.; Mankowski, L. S.; Cameron, C. E.; Fuller, F. J.; Payne, S. L. *Biochim. Biophys. Acta, Protein Struct. Mol. Enzymol.* **1997**, *1339*, 181−91.

(29) Vertessy, B. G. *Proteins: Struct., Funct., Genet.* **1997**, *28*, 568−79.

(30) Vertessy, B. G.; Larsson, G.; Persson, T.; Bergman, A. C.; Persson, R.; Nyman, P. O. *FEBS Lett.* **1998**, *421*, 83−8.

(31) Nord, J.; Kiefer, M.; Adolph, H. W.; Zeppezauer, M. M.; Nyman, P. O. *FEBS Lett.* **2000**, *472*, 312−6.

(32) Freeman, L.; Buisson, M.; Tarbouriech, N.; Van der Heyden, A.; Labbe, P.; Burmeister, W. P. *J. Biol. Chem.* **2009**, *284*, 25280−9.

(33) Barabás, O.; Németh, V.; Bodor, A.; Perczel, A.; Rosta, E.; Kele, Z.; Zagyva, I.; Szabadka, Z.; Grolmusz, V. I.; Wilmanns, M.; Vértessy, B. G. *Nucleic Acids Res.* **2013**, *41*, 10542−10555.

(34) Zabrodsky, H.; Peleg, S.; Avnir, D. *J. Am. Chem. Soc.* **1992**, *114*, 7843−7851.

(35) Palermo, G.; Cavalli, A.; Klein, M. L.; Alfonso-Prieto, M.; Dal Peraro, M.; De Vivo, M. *Acc. Chem. Res.* **2015**, 220−228.

(36) Prasad, G. S.; Stura, E. A.; Elder, J. H.; Stout, C. D. *Acta Crystallogr., Sect. D: Biol. Crystallogr.* **2000**, *56*, 1100−9.

(37) Brooks, B. R.; Bruccoleri, R. E.; Olafson, B. D.; States, D. J.; Swaminathan, S.; Karplus, M. *J. Comput. Chem.* **1983**, *4*, 187−217.

(38) Jo, S.; Kim, T.; Iyer, V. G.; Im, W. *J. Comput. Chem.* **2008**, *29*, 1859−1865.

(39) Shao, Y.; Molnar, L. F.; Jung, Y.; Kussmann, J.; Ochsenfeld, C.; Brown, S. T.; Gilbert, A. T.; Slipchenko, L. V.; Levchenko, S. V.; O'Neill, D. P.; DiStasio, R. A., Jr.; Lochan, R. C.; Wang, T.; Beran, G. J.; Besley, N. A.; Herbert, J. M.; Lin, C. Y.; Van Voorhis, T.; Chien, S. H.; Sodt, A.; Steele, R. P.; Rassolov, V. A.; Maslen, P. E.; Korambath, P. P.; Adamson, R. D.; Austin, B.; Baker, J.; Byrd, E. F.; Dachsel, H.; Doerksen, R. J.; Dreuw, A.; Dunietz, B. D.; Dutoi, A. D.; Furlani, T. R.; Gwaltney, S. R.; Heyden, A.; Hirata, S.; Hsu, C. P.; Kedziora, G.; Khalliulin, R. Z.; Klunzinger, P.; Lee, A. M.; Lee, M. S.; Liang, W.; Lotan, I.; Nair, N.; Peters, B.; Proynov, E. I.; Pieniazek, P. A.; Rhee, Y. M.; Ritchie, J.; Rosta, E.; Sherrill, C. D.; Simmonett, A. C.; Subotnik, J. E.; Woodcock, H. L., 3rd; Zhang, W.; Bell, A. T.; Chakraborty, A. K.; Chipman, D. M.; Keil, F. J.; Warshel, A.; Hehre, W. J.; Schaefer, H. F., 3rd; Kong, J.; Krylov, A. I.; Gill, P. M.; Head-Gordon, M. *Phys. Chem. Chem. Phys.* **2006**, *8*, 3172−91.

(40) Becke, A. *J. Chem. Phys.* **1993**, *98*, 5648−5652.

(41) Woodcock, H. L., 3rd; Hodoscek, M.; Gilbert, A. T.; Gill, P. M.; Schaefer, H. F., 3rd; Brooks, B. R. *J. Comput. Chem.* **2007**, *28*, 1485−502.

(42) Rosta, E.; Woodcock, H. L.; Brooks, B. R.; Hummer, G. *J. Comput. Chem.* **2009**, *30*, 1634−41.

(43) Rosta, E.; Nowotny, M.; Yang, W.; Hummer, G. *J. Am. Chem. Soc.* **2011**, *133*, 8934−41.

(44) Chu, J.-W.; Trout, B. L.; Brooks, B. R. *J. Chem. Phys.* **2003**, *119*, 12708−12717.

(45) Frisch, M. J.; Trucks, G. W.; Schlegel, H. B.; Scuseria, G. E.; Robb, M. A.; Cheeseman, J. R.; Scalmani, G.; Barone, V.; Mennucci, B.; Petersson, G. A.; Nakatsuji, H.; Caricato, M.; Li, X.; Hratchian, H. P.; Izmaylov, A. F.; Bloino, J.; Zheng, G.; Sonnenberg, J. L.; Hada, M.; Ehara, M.; Toyota, K.; Fukuda, R.; Hasegawa, J.; Ishida, M.; Nakajima, T.; Honda, Y.; Kitao, O.; Nakai, H.; Vreven, T.; Montgomery, J. A.; Peralta, J. E.; Ogliaro, F.; Bearpark, M.; Heyd, J. J.; Brothers, E.; Kudin, K. N.; Staroverov, V. N.; Kobayashi, R.; Normand, J.; Raghavachari, K.; Rendell, A.; Burant, J. C.; Iyengar, S. S.; Tomasi, J.; Cossi, M.; Rega, N.; Millam, J. M.; Klene, M.; Knox, J. E.; Cross, J. B.; Bakken, V.; Adamo, C.; Jaramillo, J.; Gomperts, R.; Stratmann, R. E.; Yazyev, O.; Austin, A. J.; Cammi, R.; Pomelli, C.; Ochterski, J. W.; Martin, R. L.; Morokuma, K.; Zakrzewski, V. G.; Voth, G. A.; Salvador, P.; Dannenberg, J. J.; Dapprich, S.; Daniels, A. D.; Farkas; Foresman, J. B.; Ortiz, J. V.; Cioslowski, J.; Fox, D. J. *Gaussian 09*, revision B.01; Gaussian, Inc.: Wallingford, CT, 2009.

(46) Breneman, C. M.; Wiberg, K. B. *J. Comput. Chem.* **1990**, *11*, 361−373.

(47) Singh, U. C.; Kollman, P. A. *J. Comput. Chem.* **1984**, *5*, 129−145.

(48) Pastor, R. W.; Brooks, B. R.; Szabo, A. *Mol. Phys.* **1988**, *65*, 1409−1419.

(49) Palmen, L. G.; Becker, K.; Bulow, L.; Kvassman, J. O. *Biochemistry* **2008**, *47*, 7863−74.

(50) Garcia-Nafria, J.; Timm, J.; Harrison, C.; Turkenburg, J. P.; Wilson, K. S. *Acta Crystallogr., Sect. D: Biol. Crystallogr.* **2013**, *69*, 1367−1380.

(51) Barabas, O.; Pongracz, V.; Kovari, J.; Wilmanns, M.; Vertessy, B. G. *J. Biol. Chem.* **2004**, *279*, 42907−15.

(52) Siggaard, J. H.; Johansson, E.; Vognsen, T.; Helt, S. S.; Harris, P.; Larsen, S.; Willemoes, M. *Arch. Biochem. Biophys.* **2009**, *490*, 42−9.

(53) Florián, J.; Warshel, A. *J. Phys. Chem. B* **1998**, *102*, 719−734.

(54) Zhang, Z.; Eloge, J.; Florián, J. *Biochemistry* **2014**, *53*, 4180−4191.

(55) Klahn, M.; Rosta, E.; Warshel, A. *J. Am. Chem. Soc.* **2006**, *128*, 15310−15323.

(56) Larsson, G.; Nyman, P. O.; Kvassman, J. O. *J. Biol. Chem.* **1996**, *271*, 24010−6.

(57) Lassila, J. K.; Zalatan, J. G.; Herschlag, D. *Annu. Rev. Biochem.* **2011**, *80*, 669−702.

(58) Di Sabato, G.; Jencks, W. P. *J. Am. Chem. Soc.* **1961**, *83*, 4400−4405.

(59) Kirby, A. J.; Varvoglis, A. G. *J. Am. Chem. Soc.* **1967**, *89*, 415−423.

(60) Gorenstein, D. G.; Lee, Y. G.; Kar, D. *J. Am. Chem. Soc.* **1977**, *99*, 2264−2267.

(61) Ghysels, A.; Woodcock, H. L.; Larkin, J. D.; Miller, B. T.; Shao, Y.; Kong, J.; Neck, D. V.; Speybroeck, V. V.; Waroquier, M.; Brooks, B. R. *J. Chem. Theory Comput.* **2011**, *7*, 496−514.

(62) Klahn, M.; Braun-Sand, S.; Rosta, E.; Warshel, A. *J. Phys. Chem. B* **2005**, *109*, 15645−15650.

(63) Oláh, J.; Mulholland, A. J.; Harvey, J. N. *Proc. Natl. Acad. Sci. U. S. A.* **2011**, *108*, 6050−6055.

(64) Berezhkovskii, A. M.; Tofoleanu, F.; Buchete, N.-V. *J. Chem. Theory Comput.* **2011**, *7*, 2370−2375.

(65) Casanova, D.; Cirera, J.; Llunell, M.; Alemany, P.; Avnir, D.; Alvarez, S. *J. Am. Chem. Soc.* **2004**, *126*, 1755−1763.

(66) Alvarez, S.; Alemany, P.; Casanova, D.; Cirera, J.; Llunell, M.; Avnir, D. *Coord. Chem. Rev.* **2005**, *249*, 1693−1708.

(67) Tuvi-Arad, I.; Rozgonyi, T.; Stirling, A. *J. Phys. Chem. A* **2013**, *117*, 12726−12733.

(68) Pontikis, G.; Borden, J.; Martínek, V. c.; Florián, J. *J. Phys. Chem. A* **2009**, *113*, 3588−3593.

(69) Tóth, J.; Varga, B.; Kovács, M.; Málnási-Csizmadia, A.; Vértessy, B. G. *J. Biol. Chem.* **2007**, *282*, 33572−33582.

(70) Steitz, T. A.; Steitz, J. A. *Proc. Natl. Acad. Sci. U. S. A.* **1993**, *90*, 6498.

(71) Friedhoff, P.; Franke, I.; Meiss, G.; Wende, W.; Krause, K. L.; Pingoud, A. *Nat. Struct. Mol. Biol.* **1999**, *6*, 112−113.

(72) Kühlmann, U. C.; Moore, G. R.; James, R.; Kleanthous, C.; Hemmings, A. M. *FEBS Lett.* **1999**, *463*, 1−2.

(73) Ton-Hoang, B.; Guynet, C.; Ronning, D. R.; Cointin-Marty, B.; Dyda, F.; Chandler, M. *EMBO J.* **2005**, *24*, 3325−3338.

(74) Barabas, O.; Ronning, D. R.; Guynet, C.; Hickman, A. B.; Ton-Hoang, B.; Chandler, M.; Dyda, F. *Cell* **2008**, *132*, 208−220.

(75) Bastidas, A. C.; Deal, M. S.; Steichen, J. M.; Keshwani, M. M.; Guo, Y.; Taylor, S. S. *J. Mol. Biol.* **2012**, *422*, 215−229.

(76) Rosta, E.; Yang, W.; Hummer, G. *J. Am. Chem. Soc.* **2014**, *136*, 3137−3144.

(77) Beauge, L.; Campos, M. A. *Biochim. Biophys. Acta, Biomembr.* **1983**, *729*, 137−149.

(78) Skou, J. C. *Biochim. Biophys. Acta* **1957**, *23*, 394−401.

(79) Fukushima, Y.; Post, R. L. *J. Biol. Chem.* **1978**, *253*, 6853−6862.

(80) Knauf, P. A.; Proverbio, F.; Hoffman, J. F. *J. Gen. Physiol.* **1974**, *63*, 324−336.

(81) Collins, K.; Sellers, J. R.; Matsudaira, P. *J. Cell Biol.* **1990**, *110*, 1137−47.

(82) Ryves, W. J.; Dajani, R.; Pearl, L.; Harwood, A. J. *Biochem. Biophys. Res. Commun.* **2002**, *290*, 967−972.

(83) Lu, S.-Y.; Huang, Z.-M.; Huang, W.-K.; Liu, X.-Y.; Chen, Y.-Y.; Shi, T.; Zhang, J. *Proteins: Struct., Funct., Genet.* **2013**, *81*, 740−753.

(84) Deweese, J. E.; Osheroff, N. *Metallomics* **2010**, *2*, 450−459.

(85) Gerlits, O.; Waltman, M. J.; Taylor, S.; Langan, P.; Kovalevsky, A. *Biochemistry* **2013**, *52*, 3721−3727.

(86) Florian, J.; Goodman, M. F.; Warshel, A. *J. Am. Chem. Soc.* **2003**, *125*, 8163−77.

(87) Mones, L.; Tang, W. J.; Florian, J. *Biochemistry* **2013**, *52*, 2672−82.

(88) Duarte, F.; Aqvist, J.; Williams, N. H.; Kamerlin, S. C. *J. Am. Chem. Soc.* **2015**, *137*, 1081−93.

(89) Guthrie, J. P. *J. Am. Chem. Soc.* **1977**, *99*, 3991−4001.

(90) Meyer, E. A.; Castellano, R. K.; Diederich, F. *Angew. Chem., Int. Ed.* **2003**, *42*, 1210−1250.

(91) Guo, X.; Chen, X.; Weber, I. T.; Harrison, R. W.; Tai, P. C. *Biochemistry* **2006**, *45*, 14473−80.

(92) Rickert, K. W.; Schaber, M.; Torrent, M.; Neilson, L. A.; Tasber, E. S.; Garbaccio, R.; Coleman, P. J.; Harvey, D.; Zhang, Y.; Yang, Y.; Marshall, G.; Lee, L.; Walsh, E. S.; Hamilton, K.; Buser, C. A. *Arch. Biochem. Biophys.* **2008**, *469*, 220−31.

(93) Boehr, D. D.; Farley, A. R.; Wright, G. D.; Cox, J. R. *Chem. Biol.* **2002**, *9*, 1209−17.

(94) Sinnokrot, M. O.; Sherrill, C. D. *J. Am. Chem. Soc.* **2004**, *126*, 7690−7.

(95) Lans, I.; Medina, M.; Rosta, E.; Hummer, G.; Garcia-Viloca, M.; Lluch, J. M.; González-Lafont, À. *J. Am. Chem. Soc.* **2012**, *134*, 20544−20553.

(96) Castro, C.; Smidansky, E.; Maksimchuk, K. R.; Arnold, J. J.; Korneeva, V. S.; Gotte, M.; Konigsberg, W.; Cameron, C. E. *Proc. Natl. Acad. Sci. U. S. A.* **2007**, *104*, 4267−4272.

(97) Ganguly, A.; Thaplyal, P.; Rosta, E.; Bevilacqua, P. C.; Hammes-Schiffer, S. *J. Am. Chem. Soc.* **2014**, *136*, 1483−1496.

(98) Wang, J.; Yang, W. *J. Phys. Chem. B* **2013**, *117*, 9354−9361.